EXPERIMENTAL STUDY OF THE INFLUENCE OF THE SHAPE ON THE SPANWISE COHERENCE LENGTH OF THE FLOW OVER A BLUFF BODY

Wagner José Gonçalves da Silva Pinto[1] **Florent Margnat**[1] **Camille Noûs**[2]
[1] Institut PPrime, CNRS - Université de Poitiers - ISAE-ENSMA, France
[2] Laboratoire Cogitamus
florent.margnat@univ-poitiers.fr

ABSTRACT

The coherence length is a key ingredient in the efficiency of the aeolian tone generated by the flow over a bluff body, and is often used to extrapolate noise simulations of a short segment of cylinder for comparison with measurements using longer bodies. In the present study, the influence of the cylinder cross-section on the coherence length is studied experimentally in BETI wind tunnel, by hot-wire anemometry of the flow over a circular, a square and two rectangular cylinders, at Reynolds number from 6,700 to 27,000. The coherence length estimation method is first validated for the circular cylinder case, in agreement with values obtained from wall-pressure measurement in the literature. The mean flow is then scanned for the rectangular sections, and the locations of the probes for the spanwise study are based on its topology, such as the position of maximum velocity. This ensures fair comparisons between the geometries, while, finally, having no qualitative influence on the coherence length value. For the square cylinder, the coherence length at the peak frequency is close to, though a little higher than, that of the circular cylinder. For the rectangular cylinder, coherence lengths up to 20 diameters are measured at the peak frequency. Considering the length of the model and the size of the test-section, these high values leads to the conclusion that the shear-layer flapping is a 2D dynamics at these regimes.

1. INTRODUCTION

The present study [1] aims at characterizing the influence of shape on bluff body aeroacoustics. The spanwise coherence length is one of the two major ingredients of the acoustic intensity of aeolian tones [2], the other one being the sectional aerodynamic force. Experimental values for the spanwise coherent length are only mentioned in the literature for the circular cylinder flow [**?**, 3, 4]. In the present study, the spanwise coherent length is estimated for a circular cylinder, a square cylinder, and two rectangular cylinders, for Reynolds numbers between 6,700 and 27,000. Thus, the present results provides an insight in how the Reynolds number and the shape of the body influences the spanwise coherence: it is shown that if the velocity does not change it much in the tested range, the known value for the circular cylinder is not universal to other shapes.

The spanwise distribution is here investigated by hotwire anemometry (HWA). Its intrusive character and incorrectness in reverse flow regions notwithstanding, one may wonder how representative of wall flow topology the HWA result is. The reviews done by Ribeiro [5] and Norberg [6] present several methods for quantifying the flow spanwise signature, and they affirm that the analysis of velocity data returns the same values as the ones obtained from surface pressure. At the same time, velocity probes can be moved freely to any spanwise station and there is no limitation regarding the size and number of the obstacles, which need not to be instrumented.

This paper is presented as follows. In Section 2, the experimental setup, the signal processing and the validation of the methodology to estimate the coherence length are presented. In Section 3, results for the square and rectangular cylinders are discussed.

2. COHERENCE LENGTH ESTIMATION METHODOLOGY

2.1 Experimental setup

2.1.1 Test facility and anemometry

This work was performed in the anechoic wind tunnel BETI of Institut PPRIME, at Poitiers, France. It is of closed circuit, with an exit nozzle of section 70 cm $\times$ 70 cm, contraction factor of 10 and an open test section. The maximum velocity is 60 m/s. The turbulent intensity at the center of the jet is of 0.5%.

Hot-wire anemometry is performed using Dantec P11 one-dimensional probes and a NI-4472 acquisition plate. The system is re-calibrated before each measuring session and a 4^{th} order polynomial law is used for converting the voltage into velocity. Due to the nature of the curve, the calibration law imposes a minimum velocity of around 5 m/s and the obtained voltage at smaller values will return highly underestimated or overestimated quantities.

Measurements with fixed and moving probes are performed. The fixed hot-wire is connected to a placing system attached to the upper edge of the nozzle, while the moving hot-wire probe is connected to a 3-axis arm via a profiled support. For measurements at U_∞ = 40 m/s, the

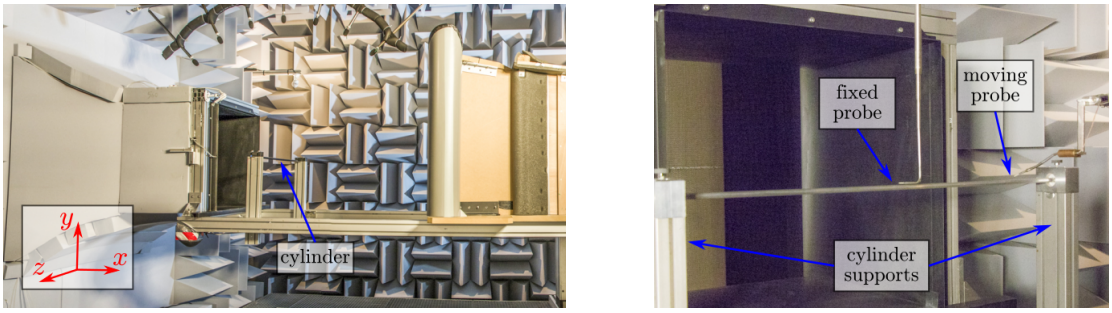

Figure 1. Wind tunnel facility BETI at Institut PPRIME, at Poitiers, France. General (left) and close-up (right) view.

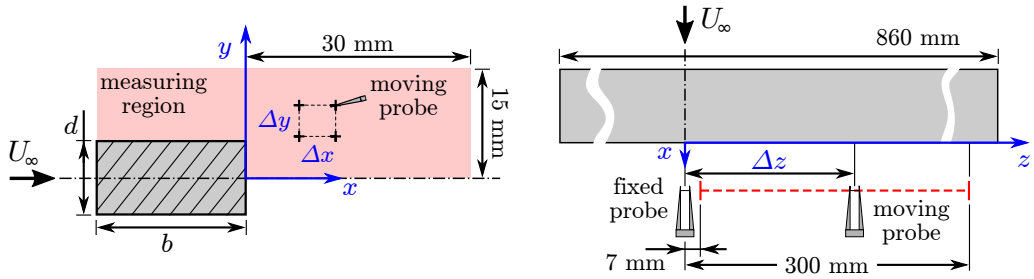

Figure 2. Diagrams of the experimental setups for obtaining the mean velocity fields (left) and the spanwise coherence (right).

positions in x and y may lose precision, because the vibrations of the arm that supports the moving hot-wire are of magnitude of 1 mm.

The wind-tunnel facility and the setup with the hot-wire probe and support are illustrated on Figure 1. The coordinate system is also highlighted, with x following the flow direction, y in the transverse axis and z in the cylinders axis direction. For simplicity and based on the fact that spanwise flow symmetry is assumed, the sign of z is ignored when presenting the results, so z = 30 mm actually means z = -30 mm.

2.1.2 Models

Tested geometries are cylinders with different cross sections (with fixed height of d = 10 mm, that is 1.4% blockage): circular cylinder; square cylinder; rectangular cylinder of dimension $d \times b = 10$ mm $\times$ 20 mm; and rectangular section of dimension $d \times b = 10 \times 30$ mm. The aspect ratio, defined as the ratio between the section height and breadth, $\mathrm{AR} = b/d$, are thus of 1, 2 and 3, respectively. The angle of attack of the rectangular sections is constant, fixed at 0° (with a precision of 0.1°, measured on a single side of the cylinder).

The obstacles are fixed at a streamwise distance of 30 cm from the outlet of the nozzle. They are supported by two vertical bars at the two spanwise limits of the cylinder. Considering the region between the supports, the total geometrical length of the cylinder is of 86 cm; no end plate or any other technique is applied to minimize the influence of the sides on the flow, thus this is not the actual length in terms of flow aerodynamics. The latter is indeed about that of the jet, $\approx 70d$, with uncertainties due to the mixing layers.

2.1.3 Flow configurations

Considering the height d as the length scale, the Reynolds number $Re = U_\infty d/\nu$ is the same for all geometries at a given flow velocity; similarly, d is used as reference for the Strouhal number $\mathrm{St} = fd/U_\infty$. The room temperature and the wind tunnel velocity at the nozzle are also recorded. Considering all performed measurements, the air temperature varies between 17.4 and 22.8 degrees Celsius with an average of 19.7 $°C$. For simplicity, the air viscosity of $\nu = 1.5 \times 10^{-5}\mathrm{m}^2/\mathrm{s}$ is selected and used independently of the measured temperature in every specific session, what gives a Reynolds number range of 6,700 to 27,000. Effects on air compressibility remain negligible for the tested velocities, with a Mach number range of 0.03 to 0.12.

2.1.4 Probe positions and parameters

Two different groups of measurements are conducted successively:

- The mean, homogeneous, flow topology is first obtained via velocity magnitude recordings in a XY plan using the 3-axis robot. This is used to set the relevant XY positions where the spanwise study shall be conducted afterwards. As depicted in Figure 2(left), the measuring zone starts from the upstream limit of the section (x = -d = -10, -20 and -30 mm) to x = +30 mm. In y, the lower limit is the symmetry line of the section (y = 0 mm), and upper limit is $y = 3d$ = 15 mm. At the center of the cylinder (z = 0) a grid of Δx = 1 mm and Δy = 2 mm is used, resulting in: 294 acquisition points for the smaller section (AR = 1); 339 for AR = 2; and to 384 for the longest rectangle (AR = 3). The same

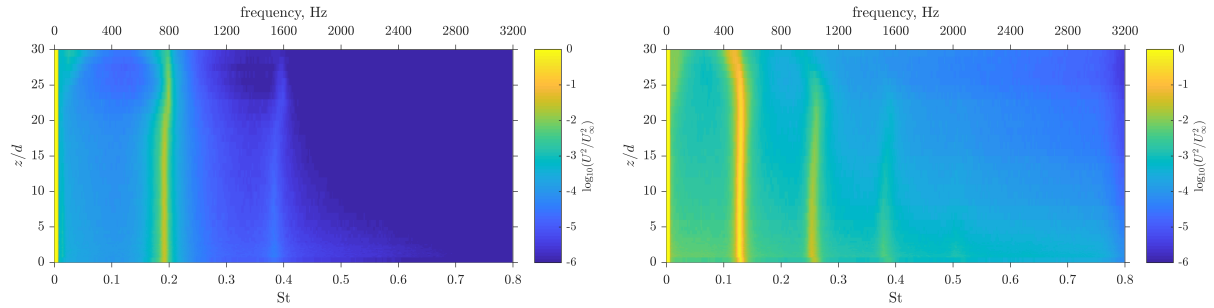

Figure 3. Spanwise distribution of the velocity spectral power density for the circular (left, probe at $(x, y) = (+0.0d, +0.9d)$) and square (right, probe at P_4, see Section 3.1.2) cylinders, at $\mathrm{Re} = 27,000$.

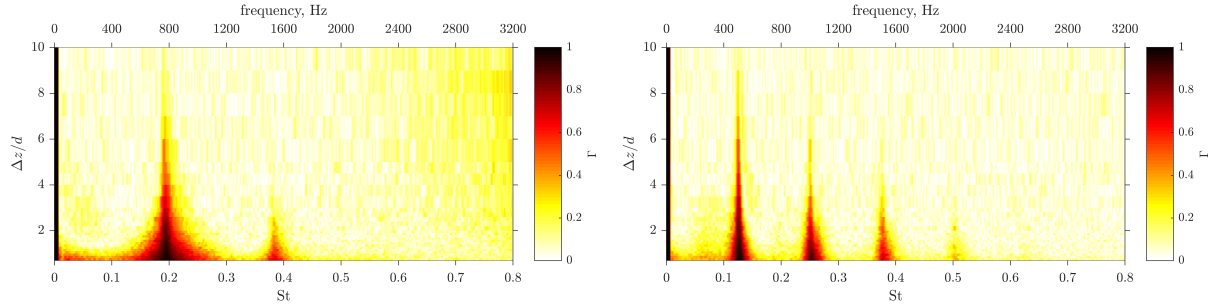

Figure 4. Spanwise coherence of the velocity in the flow over the circular (left, probe at $(x, y) = (+0.0d, +0.9d)$) and square (right, probe at P_4, see Section 3.1.2) cylinders, at $\mathrm{Re} = 27,000$.

measurement is performed at two different plans (z = 150 mm and z = 300 mm), with less points (Δx = 2 mm), composing meshes of 144, 164 and 184 points, from the shortest to longest rectangular section, in order to assess spanwise consistency of the flow topology. Since only the mean flow is investigated, the acquisition frequency is chosen as 1 kHz and the sampling duration is of 5 seconds.

- Velocity magnitude measurements are next carried out with the same moving hot-wire probe but now in the spanwise direction at fixed XY coordinates, as shown in Figure 2(right). For performing coherence and correlation calculations, a fixed probe is simultaneously recording the velocity at the cross symmetry plan of the cylinder ($z = 0$ mm). Due to the presence of the supports of the hot-wires, the starting point of the moving probe is at a spanwise distance of $\Delta z = 0.7d$ = 7 mm from the fixed probe. A total of 48 spanwise positions are used, up to z = 300 mm. Aiming at a spectral analysis, larger acquisition frequency and time of 6.4 kHz and 30 seconds are selected, respectively. Considering a spectral peak at Strouhal number of 0.2, the acquisition time thus covers at least 6000 cycles of the main unsteady mode.

2.2 Signal processing

2.2.1 Peak frequency estimation

Spectra are estimated with the Welch periodogram method, adjusting the size of segments to have the same frequency resolution $\Delta\mathrm{St} = 0.001$ for all velocities. In order to improve peak localization, the segments are zero-padded to double their size while Chebyshev window with 100 dB attenuation of the secondary lobes is selected. Two examples are given in Figure 3 for the circular and square cylinder flows at $U_\infty = 40$ m/s. They, as all of the other cases, exhibit one main peak typically for St between 0.12 and 0.20. This is refered to as the main frequency ($\mathrm{St}_{\mathrm{peak}}$). A good homogeneity of the flow is noticed for $|z| \leq 20d$, while there is a slight variation of $\mathrm{St}_{\mathrm{peak}}$ beyond, illustrating end effects. The harmonics appear more energetic for the square section. The mathematical procedure used for the quantitative description of the spanwise behavior of the flow is presented next.

2.2.2 Spanwise coherence

Considering two signals u_i and u_j of a flow quantity u recorded simultaneously at spanwise locations z_i and z_j respectively, the coherence between u_i and u_j is calculated as:

$$\Gamma_{s,ij}(\omega) = \Gamma_s(\eta, \omega) = \frac{\left|\overline{s}_i \overline{s}_j^*\right|}{\sqrt{\overline{s}_i^2}\sqrt{\overline{s}_j^2}} \qquad (1)$$

where ω is a frequency quantity, $\eta = \Delta z/d = (z_j - z_i)/d$ is the normalized spanwise lag, $\overline{u}_i$ and $\overline{u}_j$ are the Fourier transform of the fluctuation of u_i and u_j, and the superscript $*$ indicates the complex conjugate, while $|\cdot|$ is the modulus. The coherence calculations are based on averaged spectra density, using the same settings as for the velocity spectra calculation.

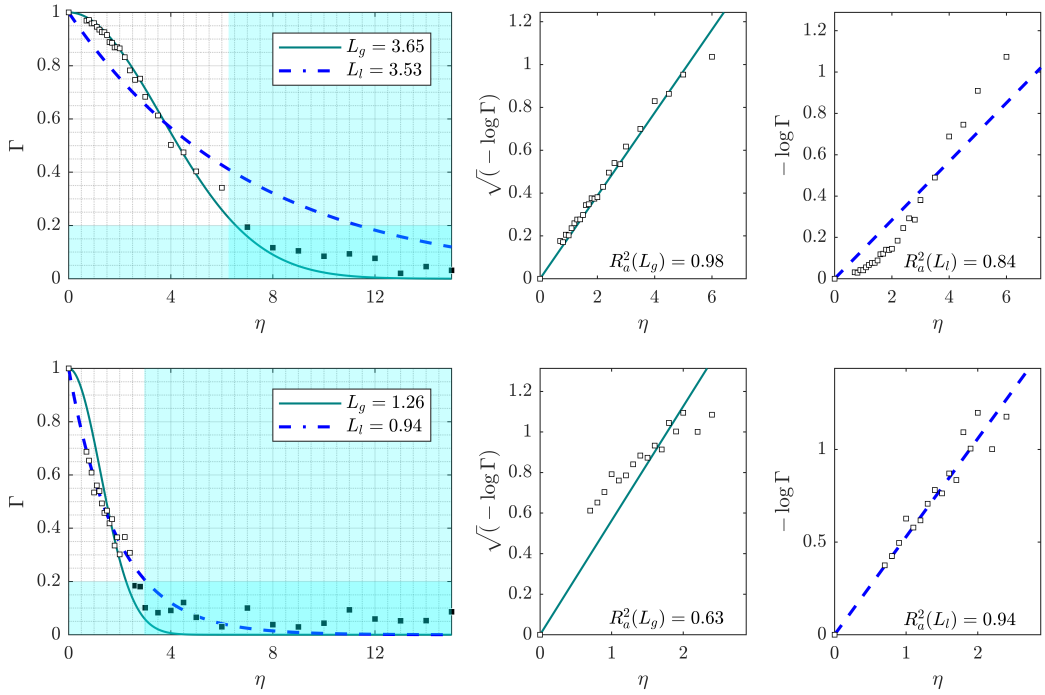

Figure 5. Spanwise coherence data (symbols) and its modelling at the lift (top, $\mathrm{St} = 0.193$) and drag (bottom, $\mathrm{St} = 0.383$) peak frequencies, for the circular section at $\mathrm{Re} = 27,000$. Data within the cyan colored regions are excluded from the regressions. On the right panels, the linear regressions of the included data for the Gaussian (full line) and Laplacian (dashed line) modellings are plotted, with indication of the corresponding adjusted determination coefficient R_a.

Maps of spanwise coherence, that is $\Gamma_u(\eta, \omega)$ fields, are plotted in Figure 4 for the circular and square cylinder flow at $U_\infty = 40$ m/s. For the square section, the peaks are sharper and coherence emerges from the background noise up to the third harmonic, while for the circular section, only the lift and drag main peaks are visible.

2.2.3 *Modelling of the coherence decay*

The coherence value for $\eta = 0$ (the test of the signal with itself) is unitary by construction. For most of the peak frequencies, the evolution of Γ_u with η follows well a Gaussian probability density:

$$\tilde{\Gamma}(\eta, \omega) = \exp\left(-\frac{\eta^2}{2L_g(\omega)^2}\right) \tag{2}$$

where $\tilde{\Gamma}$ denotes the modelling of the coherence function, and L_g is the Gaussian coherence length, normalized by the diameter. Such modelling reduces the coherence, bi-point spanwise, data to a single value, the coherence length. The latter can be evaluated by fitting the data $\Gamma_u(\eta)$ for a given frequency, that is, performing linear regression between $\sqrt{-\log(\Gamma_u(\eta))}$ and η. Since the point $\Gamma(\eta = 0) = 1$ is known by construction, this reduces to evaluate one single regression coefficient α such that:

$$\sqrt{-\log(\Gamma_u(\eta))} = \alpha\, \eta \tag{3}$$

The coherence length is obtained afterwards by $L_g = 1/\sqrt{2\alpha}$

For some frequencies, the drag frequency of the circular cylinder flow for instance, the coherence decay rather follows a Laplacian distribution, that is:

$$\tilde{\Gamma}(\eta, \omega) = \exp\left(-\frac{|\eta|}{2L_l(\omega)}\right) \tag{4}$$

Then, L_l is deduced from the single regression coefficient between $-\log(\Gamma_u(\eta))$ and η.

The process is illustrated in Figure 5: coherence data for the lift and drag peak frequencies of the circular cylinder flow at $U_\infty = 40$ m/s are plotted up to $\Delta z = 15d$ (Figure 5, left). Data such that $\Gamma < 0.2$ and $\eta \geq \beta L_{0.6}$, where $L_{0.6}$ is the spanwise lag where $\Gamma_u = e^{-0.5}$ and $\beta = 1.79$ and 3.22 for the 1st and 2nd peak respectively, are excluded from the fittings. This is necessary in the present experiments which cover a large spanwise extent while the coherence data exhibit residual noise up to 0.15 due to probe uncertainties and signal processing, as visible in Figure 4. The linear regressions for both the Gaussian and Laplacian modellings are shown. A very high determination coefficient R_a^2 is obtained for the Gaussian modelling of the coherence decay at the lift peak (Figure 5, top, middle) and for the Laplacian modelling a the drag peak (Figure 5, bottom, right). In each case, the alternate modelling yields a lower R_a^2. High values of R_a^2 evidence high quality regressions only because a large number of spanwise lags are measured and because they cover the whole coherence decay.

The modelled coherence functions are then superimposed to the data in Figure 5(left) showing the clear dis-

Table 1. Configurations and coherence length (in cylinder diameters) at the peak (lift) frequency, from literature and present study, for the circular cylinder flow. The other experimental works [3, 4, 7] used wall pressure data. Maryami *et al.* estimated L_g at different circumferential angles: the range of L_g reproduced here excludes values obtained at the front and rear mean stagnation points, which are qualitatively different. Coherence length values reported in literature using different definition than (2) are converted accordingly.

reference			Re	d, mm	total span/diameter	max $\Delta z/d$	L_g
Orselli et al.	[8]	num.	$89,000$	19	2.5	0.95	6.7
Seo & Moon	[9]	num.	$46,000$	10	3	1.0	4.3
Casalino & Jacob	[3]	exp.	$22,000$	16	19	5.1	3.9
Jacob *et al.*	[7]	exp.	$13,000 - 48,000$	10	30	6.2	$3.8 - 4.9$
			$21,000 - 77,000$	16	19	5.2	$4.0 - 3.5$
Maryami *et al.*	[4]	exp.	$30,000$	22	21	6	$4.4 - 4.7$
Present work		exp.	$13,000$	10	70	30	3.7
			$20,000$				3.6
			$27,000$				3.7

tinction between the two modellings.

2.3 Validation

The present methodology yield $L_g \approx 3.6$ for the circular cylinder flow at Re around 20,000. As visible in Table 1, this is in good agreement with literature values obtained from wall pressure measurements at similar regimes. Numerical works at higher Reynolds numbers reported higher coherence length values. Further validation by comparisons to literature data of spanwise correlation and coherence is conducted in [1]. Note that the present experiment consider spanwise lags which are far larger than previous studies. As revealed by the following, this is critical to correctly address rectangular cylinder flows.

3. MEASUREMENTS FOR SQUARE AND RECTANGULAR CYLINDERS

The investigation of the spanwise characteristics of the flow is performed for cylinders of rectangular section. In a preliminary study, mean velocity fields are obtained, which are used to set the positions where to place the probes in the XY plane for the spanwise analysis. This is followed by a description of the spanwise coherence for the tested cross-sections.

3.1 Identification of fair probe locations

3.1.1 Mean velocity fields

Velocity fields in the cross plane $z = 0$ are produced with hot-wire measurements for different inflow velocities (U_∞ = 10, 20 and 40 m/s), for the different rectangular sections. Results are presented in Figure 6 for the two higher velocities. The contour line $|U|/U_\infty$ = 1, calculated using bi-linear interpolation, is also represented.

It is noted that the overall flow topology is maintained for both velocities, with a recirculation zone on the upper face of the cylinder. The chosen reference line $|U|/U_\infty$ = 1, works as an estimator of the separation layer position, starting at the upstream edge of the upper face and being expanded upstream due to the evolution of the vortex in the y direction. The size of the recirculation is modified simultaneously by the velocity and the aspect ratio, being the later parameter the most important. For the longest rectangle, it appears that the flow reattaches the upper wall, while for the shorter sections, only the initial detachment seems to exist.

Recall that for the fastest flow, the apparent displacement of the mixing layer in the $+y$ direction is probably inflated by the displacement of the hot wire support in the other sense. No correction is performed since the dislocation value is not known with precision.

Based on those mean flows, the spanwise study is conducted for a couple of positions in the XY plane that are topologically equivalent for each velocity and geometry, as describe in the following subsection 3.1.2.

3.1.2 Probe positions for the spanwise study

Following Ribeiro [5], 4 probe locations are proposed for quantifying the spanwise flow behavior:

- P_1: in the wake, fixed location $(x, y) = (d, 0)$;
- P_2: at the position of maximum average velocity;
- P_3: where the reference line is flat, in an analogy of the max y of the mixing layer;
- P_4: where the curvature of the reference line is maximal, in an analogy of the expansion of the vortex.

An illustration of the 4 measuring points is presented in Figure 7 for the square cylinder at Re = 13,000. Being in the wake, P_1 obviously does not respect the guidelines presented on [5], so it is included mainly to check the consistency of the flow. P_2, being at the position with the biggest velocity, is believed to contain a larger quantity of energy. Also, the existence of a minimal speed due to the

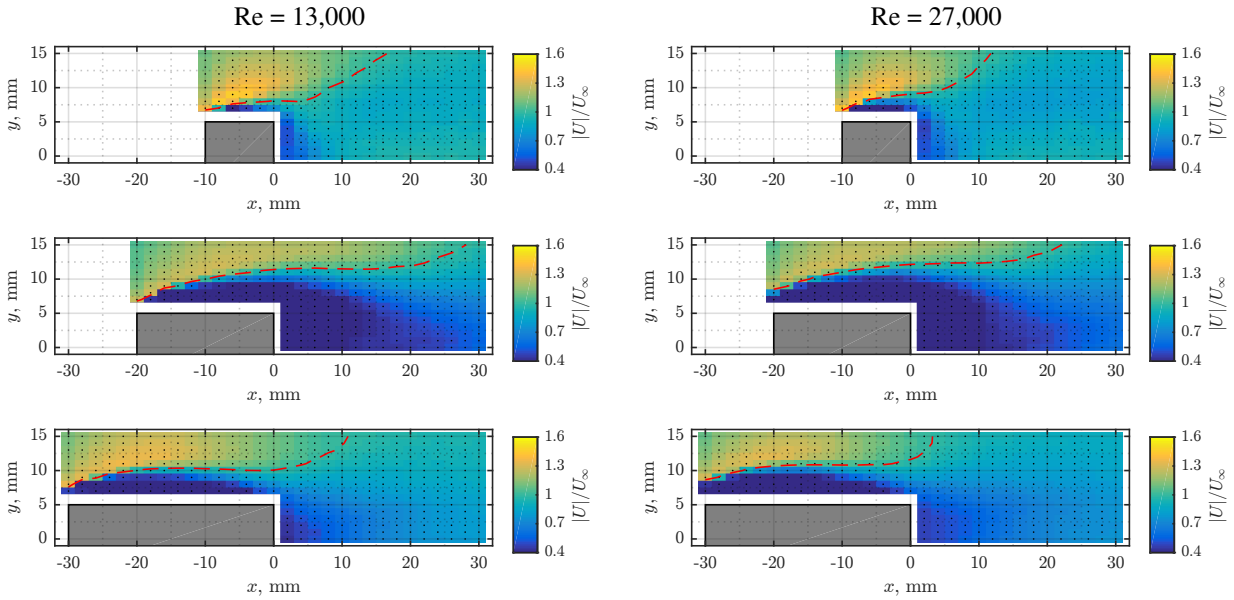

Figure 6. Mean field in the midspan halfplane for the square (top) and rectangular AR = 2 (middle) and AR = 3 (bottom) sections, at $U_\infty = 20$ m/s (left) and $U_\infty = 40$ m/s (right). Dots represent the measurement points and the dashed red line is the iso-contour of the velocity inlet ($|U|/U_\infty = 1$).

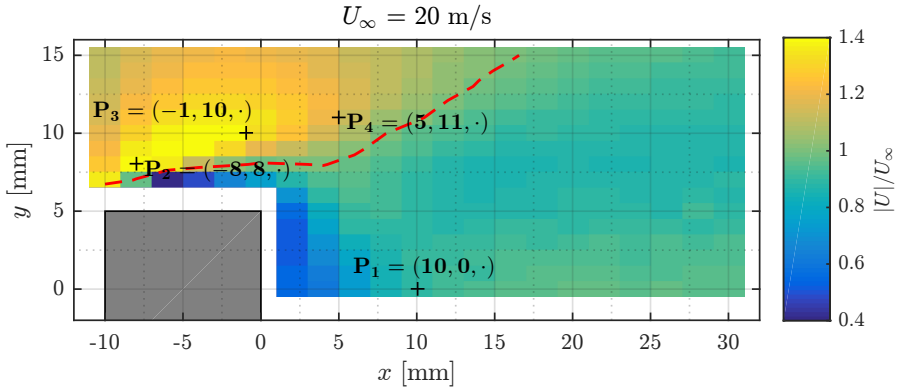

Figure 7. Mean velocity field and plan coordinates (in mm) for the spanwise analysis (square cylinder, Re = 13,000).

limitations of the measuring technique, makes a position with larger velocities a safer choice, lowering the risk of measurement bias.

3.1.3 Influence of probe position on coherence

For the square cylindre, coherence maps at P_1 and P_3 are plotted in Figure 8 at $U_\infty = 40$ m/s. These are to be compared also to Figure 4 (right) that show the field for P_4. High levels of coherence are noted at the peak Strouhal number 0.127 and its first harmonics, even for the probe in the wake (P_1) though missing harmonics above the drag peak. The increase of broadband coherence for P_3 (and for P_2, not shown), together with the appearance of intermediary modes, is believed to be due to its reduced distance to the wall, so that the impossibility to have a precise measurement at low speed and the influence of the hot-wire to the flow dynamics are likely non negligible. In spite of this, the key aspects of the flow spanwise distribution are found equally visible for the 4 tested points, being the graphical representations of the coherence obtained at P_3 and P_4 almost identical. This is in agreement with considering the vortex shedding as the development of a global instability. The same behavior is also observed at the other velocities (not shown). More plots are provided in [1].

For the rectangular sections, only P_2 and P_4 are used, for the study on the square cylinder has established that P_1 and P_3 do not bring additional information for the estimation of the coherence length. The coherence maps for the AR $= 3$ section are plotted in Figures 9 for $U_\infty = 40$ m/s. High values of Γ_s are found around St $= 0.16$ and also around St $= 0.32$, the first harmonic. For this long breadth geometry, these high levels are sustained far beyond $\Delta z = 10d$. Almost no difference is noticed between the two probe locations except that, at the harmonic, the coherence peak extents a little further for P_4 than for P_2. The high coherence at low to zero frequency may be due to the reduced strength of the unsteady mode encountered with longer sections , so the calculated values are more in-

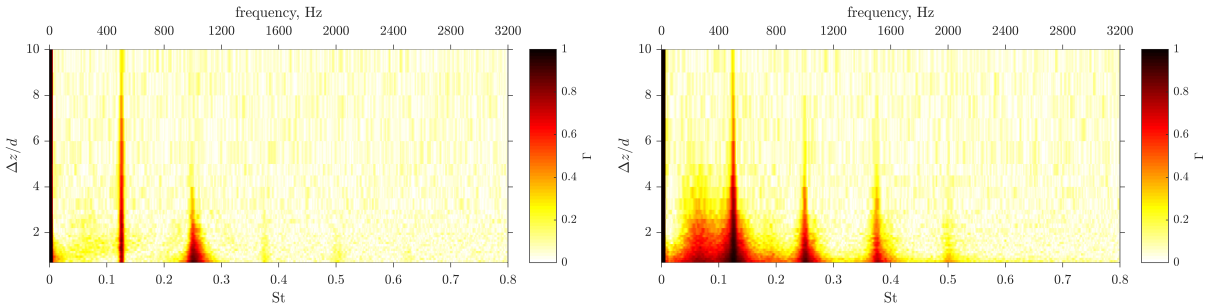

Figure 8. Spanwise coherence of the velocity around the square cylinder at $\mathrm{Re} = 27,000$. Probe at P_1 (left) and P_3 (right).

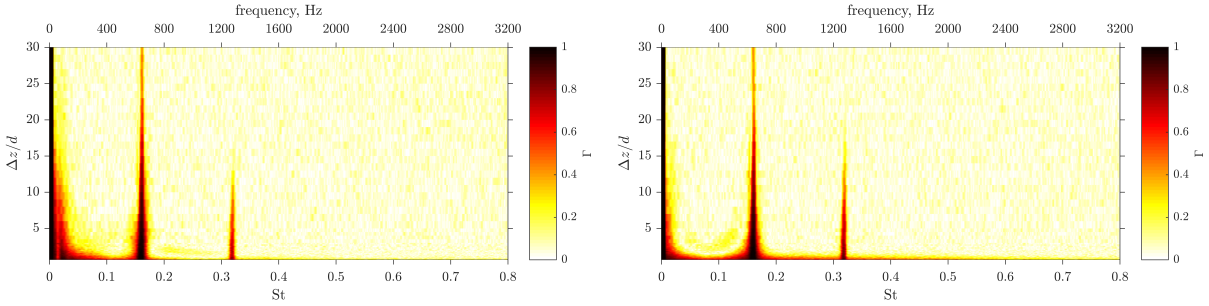

Figure 9. Spanwise coherence of the velocity in the flow over the rectangular cylinder of $\mathrm{AR} = 3$ at $\mathrm{Re} = 27,000$. Probe at P_2 (left) and P_4 (right).

fluenced by the spanwise loss of homogeneity of the mean velocity.

3.2 Coherence length for rectangular cylinders

For the three rectangular sections at $U_\infty = 40$ m/s, Figure 10 evidences the relevancy of the Gaussian modelling of coherence data at the peak frequency. For the square section, a coherence length of $L_g = 4.2$ is obtained, which is significantly higher than that of the circular cylinder at the same regime, see Figure 5 and Table 1. The fitting yields $L_g = 9.9$ and $L_g = 18.6$ for $\mathrm{AR} = 2$ and 3 respectively. These are considerably high values.

It is striking that coherence data for the longest rectangle ($\mathrm{AR} = 3$) is above 0.35 up to $\eta = 30$, that is the whole tested (half) span. Given its non-stochastic distribution and the coherence fields for the other geometries, this can definitely not be due to measurement noise, and lead to the conclusion that the flow has a two-dimensional property at this frequency.

Table 2 gathers the measured coherence length for rectangular cylinders in the present study. It is limited to the peak frequencies for which the Gaussian modelling was found relevant enough. For $\mathrm{AR} = 2$, two main peaks are noticed at $U_\infty = 40$ m/s while they are not harmonics and correspond to two flow modes depending on shear-layer reattachment on the side of the shape, as further discussed in [1]. Both modes exhibit higher coherence length than the square cylinder. Table 2 confirms that the coherence length is almost insensitive to the probe location. All fittings are of very good quality, while very large coherence lengths are noticed for the long-breadth sections at both tested velocities.

Table 2. Coherence lengths for rectangular cylinders. $\mathrm{St}_{\mathrm{peak}}$ is defined as the maximum of $\int_0^\infty \Gamma_u \mathrm{d}\eta$.

AR	probe	$\mathrm{St}_{\mathrm{peak}}$	L_g	R_a^2
Re = 6,700 (U_∞ = 10 m/s)				
1.0	P_2	0.125	3.4	0.99
	P_3	0.127	2.9	0.97
	P_4	0.128	2.6	0.97
Re = 13,000 (U_∞ = 20 m/s)				
1.0	P_2	0.125	4.6	0.98
	P_3	0.125	4.0	0.96
	P_4	0.126	3.4	0.97
2.0	P_2	0.142	10.1	0.74
	P_4	0.141	9.5	0.95
3.0	P_2	0.164	16.0	0.94
	P_4	0.164	13.8	0.96
Re = 27,000 (U_∞ = 40 m/s)				
1.0	P_2	0.128	4.9	0.97
	P_3	0.125	4.5	0.97
	P_4	0.125	4.2	0.98
2.0	P_2	0.074	11.3	0.99
	P_4	0.076	9.9	0.94
2.0	P_2	0.145	7.8	0.91
	P_4	0.146	6.1	0.90
3.0	P_2	0.161	20.1	0.96
	P_4	0.161	18.6	0.97

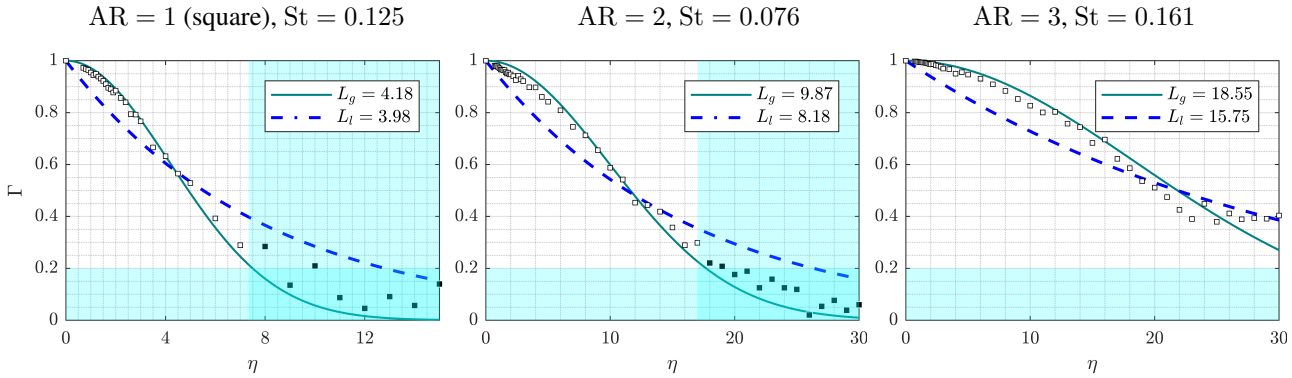

Figure 10. Spanwise coherence data at the peak frequency (symbols) and its Gaussian (full line) and Laplacian (dashed line) modellings, for the rectangular sections at $\mathrm{Re} = 27,000$ for probe at P_4. Data within the cyan colored region are excluded from the regression.

4. CONCLUSIONS

For the first time, spanwise coherence lengths have been measured in the flow over rectangular cylinders, in the regime $\mathrm{Re} \approx 20,000$. The high levels of spanwise coherence over almost the whole length of the model noticed for the rectangular cylinder of $\mathrm{AR} = 3$ may be associated with the loud and highly tonal acoustic signature that has been reported in the same facility [1, 10].

A. PROBE LOCATIONS

The coordinate system starts at the center of the downstream face of the cylinder's cross-section (see Figure 2). Spanwise measurements at P_1, fixed at $(x, y) = (1.0d, 0)$ for all velocities, and P_3 are used with the square section only. For the circular cylinder, all measurements are performed at $(x, y) = (0.0d, 0.9d)$.

Table 3. Measuring coordinates in the XY plan.

AR	P_2	P_3	P_4
Re = 6,667 (U_∞ = 10 m/s)			
1.0	(-0.6d, 0.8d)	(0.1d, 0.9d)	(0.4d, 0.9d)
Re = 13,333 (U_∞ = 20 m/s)			
1.0	(-0.8d, 0.8d)	(-0.1d, 1.0d)	(0.5d, 1.1d)
2.0	(-0.8d, 1.2d)	(1.1d, 1.4d)	(2.6d, 1.6d)
3.0	(-2.2d, 1.1d)	(-0.3d, 1.2d)	(0.6d, 1.4d)
Re = 26,667 (U_∞ = 40 m/s)			
1.0	(-1.0d, 0.7d)	(-1.0d, 1.1d)	(0.5d, 1.2d)
2.0	(-1.2d, 1.2d)	(0.6d, 1.4d)	(2.1d, 1.7d)
3.0	(-2.2d, 1.2d)	(-1.3d, 1.3d)	(-1.0d, 1.4d)

B. REFERENCES

[1] W. J. Gonçalves da Silva Pinto, *Modelling airframe noise: from aerodynamic topology to acoustic efficiency*. PhD thesis, Université de Poitiers, Oct. 2019.

[2] O. M. Phillips, "The intensity of aeolian tones," *Journal of Fluid Mechanics*, vol. 1, no. 6, p. 607–624, 1956.

[3] D. Casalino and M. Jacob, "Prediction of aerodynamic sound from circular rods via spanwise statistical modelling," *Journal of Sound and Vibration*, vol. 262, no. 4, pp. 815 – 844, 2003.

[4] R. Maryami, M. Azarpeyvand, A. A. Dehghan, and A. Afshari, "An Experimental Investigation of the Surface Pressure Fluctuations for Round Cylinders," *Journal of Fluids Engineering*, vol. 141, no. 6, 2019. 061203.

[5] J. L. D. Ribeiro, "Fluctuating lift and its spanwise correlation on a circular cylinder in a smooth and in a turbulent flow: a critical review," *Journal of Wind Engineering and Industrial Aerodynamics*, vol. 40, no. 2, pp. 179 – 198, 1992.

[6] C. Norberg, "Fluctuating lift on a circular cylinder: review and new measurements," *Journal of Fluids and Structures*, vol. 17, no. 1, pp. 57 – 96, 2003.

[7] M. C. Jacob, J. Boudet, D. Casalino, and M. Michard, "A rod-airfoil experiment as a benchmark for broadband noise modeling," *Theoretical and Computational Fluid Dynamics*, vol. 19, no. 3, 2005.

[8] R. Orselli, J. Meneghini, and F. Saltara, "Two and three-dimensional simulation of sound generated by flow around a circular cylinder," Aeroacoustics Conferences, American Institute of Aeronautics and Astronautics, May 2009.

[9] J. H. Seo and Y. J. Moon, "Aerodynamic noise prediction for long-span bodies," *Journal of Sound and Vibration*, vol. 306, no. 3, pp. 564 – 579, 2007.

[10] W. J. G. S. Pinto, F. Margnat, and Y. Gervais, "Effect of cross-section on flow three-dimensionality for prismatic bodies and the associated noise emission," in *25th AIAA/CEAS Aeroacoustics Conference (Aeroacoustics 2019), AIAA Paper 2019-2531*, (Delft, The Netherlands), 20-24 May 2019.